

Dynamic Appearance: A Video Representation for Action Recognition with Joint Training

Guoxi Huang and Adrian G. Bors

Department of Computer Science, University of York, York YO10 5GH, UK
gh825@york.ac.uk, adrian.bors@york.ac.uk

Abstract

Static appearance of video may impede the ability of a deep neural network to learn motion-relevant features in video action recognition. In this paper, we introduce a new concept, Dynamic Appearance (DA), summarizing the appearance information relating to movement in a video while filtering out the static information considered unrelated to motion. We consider distilling the dynamic appearance from raw video data as a means of efficient video understanding. To this end, we propose the Pixel-Wise Temporal Projection (PWTP), which projects the static appearance of a video into a subspace within its original vector space, while the dynamic appearance is encoded in the projection residual describing a special motion pattern. Moreover, we integrate the PWTP module with a CNN or Transformer into an end-to-end training framework, which is optimized by utilizing multi-objective optimization algorithms. We provide extensive experimental results on four action recognition benchmarks: Kinetics400, Something-Something V1, UCF101 and HMDB51.

1 Introduction

Video data is collected across both space and time, is high-dimensional and contains substantial redundancy. This is challenging to any model aiming to differentiate between relevant and irrelevant features. While leading-edge video architectures (Carreira and Zisserman 2017; Wang et al. 2018b; Feichtenhofer et al. 2019; Feichtenhofer 2020; Xie et al. 2018; Bertasius, Wang, and Torresani 2021; Fan et al. 2021) have been proposed for learning spatio-temporal features from raw video data, a quintessential spatio-temporal representation remains elusive.

The idea of characterizing movement in a video with appearance or silhouette was established early in traditional appearance-based temporal matching methods (Ahad et al. 2008; Bradski and Davis 2002). Drawing upon this, we propose a novel video representation, termed Dynamic Appearance, which summarizes the appearance information relating to movement in a video sequence while filtering out the static information considered unrelated to motion. The filtered static information that does not change from frame to frame is temporarily referred to as the Static Appearance.

Copyright © 2022, Association for the Advancement of Artificial Intelligence (www.aaai.org). All rights reserved.

To better understand the concept, we depict the dynamic appearance and static appearance of a video in Fig. 1.

Our motivation for this study stems from the observation that many videos labeled with different action categories are shot in the same environment. Taking the videos shown in Fig. 1 as an illustrative example, the two videos have different action labels ('Cricket Shot' vs. 'Cricket Bowling') but they are actually two short video clips shot in the same environment. In this case, the static appearances and scene information of these videos are very similar, describing the same object and background, which hinders deep networks that take RGB frames as input from learning relevant spatio-temporal features. In the two-stream architecture (Simonyan and Zisserman 2014), separately modeling appearance and motion by adding additional optical flow input modality could avoid the distraction caused by static appearance information. However, the computational complexity of two-stream-based architecture (Simonyan and Zisserman 2014; Feichtenhofer, Pinz, and Wildes 2016; Feichtenhofer, Pinz, and Zisserman 2016; Wang et al. 2016; Carreira and Zisserman 2017) is double that of the single-stream version. We demonstrate that a network that takes dynamic appearance as input can achieve accuracy on par with the two-stream networks while requiring less than half the computation of two-stream networks.

To disentangle the dynamic appearance from the static appearance in a video, we propose the Pixel-Wise Temporal Projection (PWTP), a lightweight and backbone-agnostic module, which is used to project the temporal information into a subspace of its original temporal dimension. The resulting projection encodes the video's static appearance while the projection residual encodes the dynamic appearance. The dynamic appearance learning enabled by PWTP can firstly be regarded as an unsupervised learning method, trained on unlabeled video data. Alternatively, we can integrate the PWTP module with a network into a unified framework, which is optimized with joint training algorithms. As a result, the framework would produce the dynamic appearance on the fly while performing action recognition. The dynamic appearance learning works as an auxiliary task to the primary recognition task. It is difficult for a network to learn action-relevant features with the recognition criteria because of the impediment of irrelevant static appearance features. However, doing this would be easier for the dy-

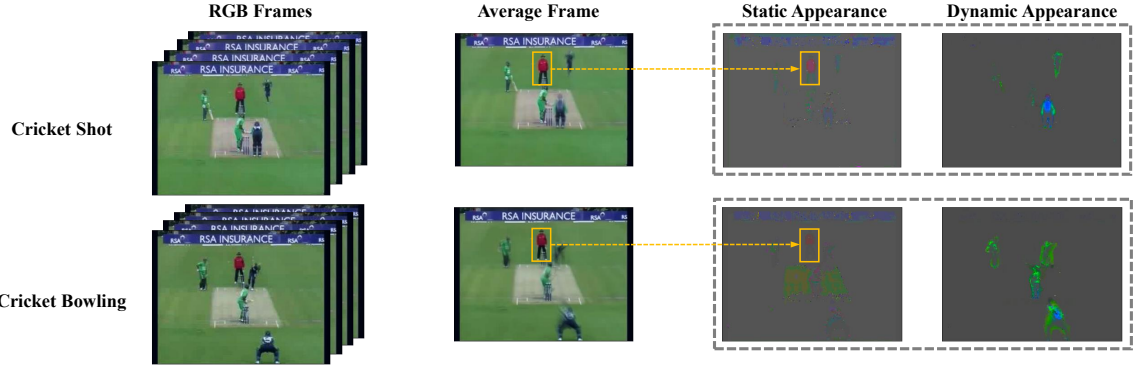


Figure 1: Different actions recorded within the same environment have very similar static appearances, which could cause confusion in classifiers. Using the Dynamic Appearance as an input resource would avoid such confusions, as it only contains the visual information related to the movement. For instance, the person in the bounding box does not move and is not included in the static appearances.

namic appearance learning task. By jointly training the two tasks, the model can better generalize on the action recognition task, as demonstrated in our experiments. We perform extensive experiments on four standard video benchmarks: Kinetics400 (Carreira and Zisserman 2017), Something-Something V1 (Goyal et al. 2017), UCF101 (Soomro, Zamir, and Shah 2012) and HMDB51 (Kuehne et al. 2011), where we show that PWTP greatly improves the performance in terms of accuracy. The experimental results successfully demonstrate that using the dynamic appearance extracted by PWTP can enable better feature learning in networks.

2 Related Work

Spatio-temporal Networks With the tremendous success of Convolutional Neural Networks(CNNs) on image classification tasks (Krizhevsky, Sutskever, and Hinton 2012; Simonyan and Zisserman 2015; Szegedy et al. 2015, 2016), various CNN-based architectures (Karpathy et al. 2014; Yue-Hei Ng et al. 2015; Wang et al. 2016; Zhu et al. 2018; Feichtenhofer, Pinz, and Zisserman 2016; Wang et al. 2017, 2021) have been proposed for spatio-temporal modeling in video recognition. Representatively, the two-stream architecture (Simonyan and Zisserman 2014) and its variants (Wang et al. 2016; Carreira and Zisserman 2017; Bilen et al. 2018; Fan et al. 2018; Zhu et al. 2018; Lin, Gan, and Han 2019) separately model appearance and motion by taking RGB video frames and the optical flow as inputs. Some published works (Taylor et al. 2010; Tran et al. 2015; Carreira and Zisserman 2017; Hara, Kataoka, and Satoh 2018) employ the computationally intensive 3D convolution to their models. Several innovative and efficient spatio-temporal networks such as P3D (Qiu, Yao, and Mei 2017), R(2+1)D (Tran et al. 2018), CSN (Tran et al. 2019) and X3D (Feichtenhofer 2020) are proposed to seek a trade-off between speed and accuracy. With the emergence of Vision Transformer (ViT) (Dosovitskiy et al. 2021), the backbone architectures in video recognition are shifted from CNNs to Transformers in recent work (Dosovitskiy et al. 2021; Berta-

sius, Wang, and Torresani 2021; Fan et al. 2021; Arnab et al. 2021).

Motion Representation Optical flow as a short-term motion representation has been widely used in action recognition. Flow Net series (Ilg et al. 2017; Dosovitskiy et al. 2015) and AutoFlow (Sun et al. 2021) improves the quality of optical flow estimation by using deep learning. Some works (Ng et al. 2018; Zhu et al. 2018) attempt to integrate optical flow estimation and the action recognition model into an end-to-end training framework. However, optical flow represents motion with instantaneous image velocities, which loses the appearance information, and therefore could cause inaccurate classification of videos in different scenes. Derived from the optical flow, OFF (Sun et al. 2018), Flow-of-Flow (Piergiovanni and Ryoo 2019) and other flow-based methods are proposed for fast motion feature learning. The seminal work (Bilen et al. 2018) utilizes the rank pooling (Fernando et al. 2015) or approximate rank pooling (Bilen et al. 2018) machine to summarize both the static and dynamic visual information of a video into a few RGB images, called dynamic images. It is worth noting that vanilla PCA cannot achieve the same result as rank pooling (Fernando et al. 2015) because PCA is a generic orthogonalization method for dimension reduction by selecting a set of orthogonal vectors, the output of which would not be adapted to the 2D or 3D layout. SVM pooling (Wang et al. 2018a) generates a video representation similar to dynamic images by exploiting the boundary information of SVM. Nevertheless, dynamic images result in poor discrimination between the moving objects and background, which harms performance when recorded videos are affected by camera shaking. Different to the existing methods, the proposed PWTP achieves the disentanglement of video's static and dynamic appearance. The dynamic appearance can be a preferable input resource to networks, encoding the temporal motion information as well as the visual information considered related to movement.

Joint Training Joint Training, one of the guises of multi-task learning, can be regarded as a form of inductive transfer, helping a model generalize better by introducing an inductive bias. Ng *et al.* (Ng et al. 2018) proposed Action-FlowNet for jointly estimating optical flow and recognizing actions. Similarly, TVNet (Fan et al. 2018) jointly trained the video representation learning and action recognition tasks. In our case, the representation learning for the static and dynamic appearance disentanglement of video is an auxiliary task to the primary action recognition task. This would allow the model to eavesdrop, *i.e.* learn the motion-relevant representation through the dynamic appearance learning task. Existing methods balance the recognition loss and the objective functions of their representation learning with some fixed scale parameters. In our study, in order to stabilize the feature learning process we analyze various joint training scenarios, such as the multiple gradient descent algorithm (Désidéri 2012).

3 Methodology

3.1 Pixel-Wise Temporal Projection

In order to achieve video static and dynamic appearance disentanglement, we propose the Pixel-Wise Temporal Projection (PWTP) operator. Given a T frame video clip \mathbf{x} of spatial resolution $H \times W$, we flatten it along the spatial dimensions, so $\mathbf{x} = \{\mathbf{x}_i\}_{i=1}^{HW}, \mathbf{x}_i \in \mathbb{R}^{T \times C}$, and C is the number of channels.

PWTP is capable of summarizing the video information from T frames into D frames, and $D \ll T$. Firstly, for every position i in the spatial dimensions, PWTP learns a particular matrix $\mathbf{A}_i \in \mathbb{R}^{T \times D}$, the column space of which defines a subspace (*i.e.* hyperplane) in \mathbb{R}^T . The columns of matrix \mathbf{A}_i are linearly independent. Then the PWTP projects \mathbf{x}_i onto the corresponding column space of \mathbf{A}_i , resulting $\hat{\mathbf{x}}_i$, given by

$$\begin{aligned} \mathbf{y}_i &= (\mathbf{A}_i^\top \mathbf{A}_i)^{-1} \mathbf{A}_i^\top \mathbf{x}_i, \\ \hat{\mathbf{x}}_i &= \mathbf{A}_i \mathbf{y}_i, \quad i = 1, \dots, HW, \end{aligned} \quad (1)$$

where $\mathbf{y} = (\mathbf{y}_1 \dots \mathbf{y}_{HW})^T, \mathbf{y}_i \in \mathbb{R}^{D \times C}$ are the mapping coefficients. Eq. (1) represents a standard projection process in the temporal dimension, which is repeatedly applied to all spatial positions. The main component of a video can be considered to be made up of the video’s static information, as the static information repeatedly appears in many frames, showing high redundancy. When the dimension of the subspace (*i.e.* $\text{rank}(\mathbf{A}_i)$) is much smaller than the original temporal dimension T in a video, its information storage capacity is significantly reduced, such that the projection output $\hat{\mathbf{x}}$ tends to encode the repeated information, characterizing static appearance that does not change from frame to frame.

The production of input-specific $\mathbf{A} = (\mathbf{A}_1 \dots \mathbf{A}_{HW})$ is realized in two steps: 1) producing a temporal relation descriptor for every spatial position i ; 2) a Multilayer Perceptron (MLP) takes as input the temporal relation descriptors and outputs the tensor \mathbf{A} . In the first step for the temporal relation description, we pass the input \mathbf{x} to a spatial convolution \mathcal{F} with the kernel size of $k \times k$ and stride of s for local

spatial information aggregation:

$$\tilde{\mathbf{x}} = \mathcal{F}_s^{k \times k}(\mathbf{x}; \theta), \quad (2)$$

where θ , of size $k \times k \times C \times C'$, denotes the kernel weights. The spatial convolution \mathcal{F} maps the tensor \mathbf{x} to $\tilde{\mathbf{x}}$ of size $\frac{HW}{s^2} \times T \times C'$, which significantly reduces the computational cost for PWTP when setting the stride $s > 1$. This is a non-trivial trick that allows the pixel-wise projection to be implemented within a feasible computation budget. Subsequently, we have $\tilde{\mathbf{x}} = \{\tilde{\mathbf{x}}_i\}_{i=1}^{HW/s^2}$ and $\tilde{\mathbf{x}}_i = \{\tilde{\mathbf{x}}_i^t\}_{t=1}^T$, where $\tilde{\mathbf{x}}_i^t \in \mathbb{R}^C$. Then, the temporal relation descriptor \mathbf{u}_i for every spatial position i is obtained as

$$\mathbf{u}_i = \left\{ \frac{1}{C'} \tilde{\mathbf{x}}_i^{t_1 \top} \tilde{\mathbf{x}}_i^{t_2} \mid t_1 \neq t_2, 1 \leq t_1, t_2 \leq T \right\}. \quad (3)$$

Consequently, \mathbf{u}_i is represented as a vector $\mathbf{u}_i \in \mathbb{R}^{\frac{T \times (T-1)}{2}}$ with ascending indices of t_1 , t_2 , and $\mathbf{u} = [\mathbf{u}_1, \dots, \mathbf{u}_{\frac{HW}{s^2}}]$. As each element in \mathbf{u}_i describes the similarity between a pair of frames, such that \mathbf{u}_i can represent the relationship between any two frames in the video clip. By taking \mathbf{u} as the input to an encoder, the projection machine would have a better understanding of the temporal relationships in the video, and so provide a better temporal projection mechanism.

The convolution $\mathcal{F}_s^{k \times k}(\cdot; \theta)$ from Eq. (2) is important for implementing temporal projection at pixel-level, as it encodes the local spatial information of each position i into the local descriptor \mathbf{u}_i , which leads to the projection result $\hat{\mathbf{x}}$ representing smooth textures. Without Eq. (2), the projection in each spatial position would be performed completely independently, which would fail to consider that the values of neighboring pixels are continuous, resulting in unsmooth spatial textures.

In the second step of the generation of \mathbf{A} , we utilize an MLP to process the temporal relation descriptors \mathbf{u} and generate \mathbf{A} :

$$\begin{aligned} \mathbf{A} &= \text{Upsample}(\text{MLP}(\mathbf{u})), \\ \text{Reshape} : \mathbf{A} &\in \mathbb{R}^{HW \times TD} \rightarrow \mathbf{A} \in \mathbb{R}^{HW \times T \times D}, \end{aligned} \quad (4)$$

where the 2D bilinear upsampling is employed in the spatial dimensions if convolution \mathcal{F} ’s stride $s > 1$. Tensor reshaping is then performed at the end. The linear independence of the columns of \mathbf{A}_i can be implemented by properly initializing the MLP (*e.g.* by avoiding to initialize all weights to zero). The MLP in the PWTP module is made up of multiple fully-connected layers with a bottleneck design where the number of features is first reduced by a factor and then recovered to its original size. The residual connection (He et al. 2016) is applied after every bottleneck. Each fully-connected layer, except for the last one, is followed by a GELU non-linearity. More details about the MLP configurations are provided in Appendix C from the Supplementary Material (SM).

3.2 Projection Residual as Dynamic Appearance

The projection residual in spatial position i is given by

$$\mathbf{p}_i = \mathbf{x}_i - \hat{\mathbf{x}}_i. \quad (5)$$

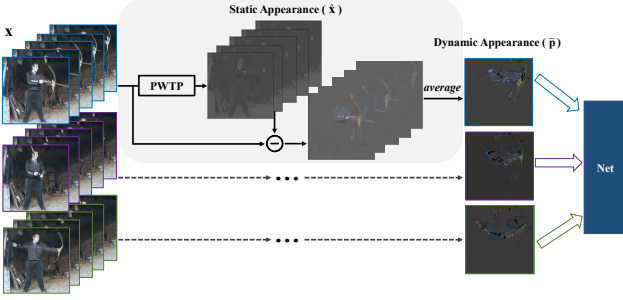


Figure 2: The video recognition framework enabled by PWTP, in which PWTP separates the dynamic appearance from the static appearance. Subsequently, the shared backbone network feeds on the dynamic appearances.

Note that when the dimension D of the subspace (*i.e.* $\text{rank}(\mathbf{A}_i)$) is much smaller than the original temporal dimension T in a video, the projection $\hat{\mathbf{x}}_i$ is forced to encode the video’s static information, because static information repeatedly appear in consecutive frames, constraining the main components of \mathbf{x}_i . Subtracting the common static features by the original \mathbf{x}_i will generate the dynamic appearance (DA). The projection residual \mathbf{p} preserves the pure dynamic appearance information of the video and filters out the static appearance. Considering that many spatial positions in the projection residual do not carry visual information after optimization, $\mathbf{p}_i \approx \mathbf{0}$, we average \mathbf{p} along the temporal direction to reduce the tensor size:

$$\bar{\mathbf{p}}_i = \frac{1}{T} \sum_{t=1}^T \mathbf{p}_i^t. \quad (6)$$

3.3 Action Recognition Framework

The recognition framework that unifies the PWTP module and a backbone network is presented in Fig. 2. We sample and then divide a video along the temporal dimension into S segments, with each segment containing T consecutive video frames. The proposed PWTP module is applied on every segment. As a result, the $S \times T$ RGB frames are projected into S frames of dynamic appearance.

By taking the dynamic appearance $\bar{\mathbf{p}}$ as input, a network can avoid the distraction caused by the static appearance ($\hat{\mathbf{x}}$) when discriminating the actions in some similar scenes, and therefore can focus on learning high-level motion-relevant features. In order to evaluate the generalization ability of our method we adapt it to different backbone architectures, including TSM R50 (Lin, Gan, and Han 2019) and X3D-XS, X3D-M (Feichtenhofer 2020) and ViT-B (Dosovitskiy et al. 2021). In order to adapt ViT-B to video applications, we duplicate the positional embedding for each segment to encode the spatio-temporal positional information. Instead of using the class token from the last layer of ViT for prediction, we average the entire sequence of embeddings from the last layer to produce the prediction. Dynamic appearance is shown experimentally to steadily improve the performance of different networks.

3.4 Joint Training

The optimization objective of PWTP is defined to minimize the Euclidean Norm of Projection Residual (ENoPR):

$$\mathcal{L}^1 = \frac{1}{HWC} \sum_{j=1}^{HWC} \|\tilde{\mathbf{p}}_j\|^2, \quad (7)$$

where $\tilde{\mathbf{p}} \in \mathbb{R}^{HWC \times T}$ denotes the flattened version of \mathbf{p} along the space and channels. \mathcal{L}^1 can be defined as a loss function $\mathcal{L}^1(\Theta^1)$ w.r.t. PWTP’s weight parameters Θ^1 . For the case of N data points, the ENoPR is expressed by:

$$\hat{\mathcal{L}}^1(\Theta^1) = \frac{1}{N} \sum_{n=1}^N \mathcal{L}_n^1(\Theta^1). \quad (8)$$

The loss function of action recognition is denoted by $\hat{\mathcal{L}}^2(\Theta^2)$ in independent training, $\hat{\mathcal{L}}^2(\Theta^1, \Theta^2)$ in joint training, where PWTP’s parameters Θ^1 are shared between the two tasks. The joint training of $\hat{\mathcal{L}}^1(\Theta^1)$ and $\hat{\mathcal{L}}^2(\Theta^1, \Theta^2)$ forms the multi-objective optimization :

$$\min_{\Theta^1, \Theta^2} \left[\alpha \hat{\mathcal{L}}^1(\Theta^1) + (1 - \alpha) \hat{\mathcal{L}}^2(\Theta^1, \Theta^2) \right], \quad 0 \leq \alpha \leq 1, \quad (9)$$

where the weight α , used to scale the contribution of the two loss functions, can be fixed, as in (Fan et al. 2018), or can be adaptive.

3.5 Multiple Gradient Descent Algorithm

For the adaptive scale α , we adopt the Multiple Gradient Descent Algorithm (MGDA) (Désidéri 2012; Sener and Koltun 2018), in which the goal of multi-objective optimization is to achieve Pareto-optimality. A solution is said to be of Pareto-stationary if and only if there is $0 \leq \alpha \leq 1$ such that:

$$\begin{aligned} \bullet & \quad \alpha \nabla_{\Theta^1} \hat{\mathcal{L}}^1(\Theta^1) + (1 - \alpha) \nabla_{\Theta^1} \hat{\mathcal{L}}^2(\Theta^1, \Theta^2) = 0, \\ \bullet & \quad \nabla_{\Theta^2} \hat{\mathcal{L}}^2(\Theta^1, \Theta^2) = 0. \end{aligned} \quad (10)$$

Pareto-stationarity is a necessary condition for Pareto-optimality. From (Désidéri 2012; Sener and Koltun 2018), the decent directions to Pareto-stationarity would be provided by solving the following optimization problem:

$$\begin{aligned} \min_{\alpha} & \quad \|\alpha \nabla_{\Theta^1} \hat{\mathcal{L}}^1(\Theta^1) + (1 - \alpha) \nabla_{\Theta^1} \hat{\mathcal{L}}^2(\Theta^1, \Theta^2)\|_2^2, \\ & \quad 0 \leq \alpha \leq 1, \end{aligned} \quad (11)$$

which is a one-dimensional quadratic function of α with an analytical solution:

$$\begin{aligned} \alpha' &= \frac{(\nabla_{\Theta^1} \hat{\mathcal{L}}^2(\Theta^1, \Theta^2) - \nabla_{\Theta^1} \hat{\mathcal{L}}^1(\Theta^1))^T \nabla_{\Theta^1} \hat{\mathcal{L}}^2(\Theta^1, \Theta^2)}{\|\nabla_{\Theta^1} \hat{\mathcal{L}}^1(\Theta^1) - \nabla_{\Theta^1} \hat{\mathcal{L}}^2(\Theta^1, \Theta^2)\|_2^2}, \\ \hat{\alpha} &= \max(\min(\alpha', 1), 0). \end{aligned} \quad (12)$$

Suppose we optimize the objective with mini-batch gradient descent, then the gradient is updated with Algorithm 1:

Algorithm 1: Optimization of the Joint Training

Input: Training tasks: $\hat{\mathcal{L}}^1(\Theta^1), \hat{\mathcal{L}}^2(\Theta^1, \Theta^2)$; Learning rate: η ;

- 1 Initialize Θ^1, Θ^2 randomly;
- 2 **while** not converged **do**
- 3 Compute gradient: $\nabla_{\Theta^1} \hat{\mathcal{L}}^1(\Theta^1)$ and $\nabla_{\Theta^1} \hat{\mathcal{L}}^2(\Theta^1, \Theta^2)$;
- 4 Update α by solving Eq. (12);
- 5 $\Theta^1 = \Theta^1 - \eta (\alpha \nabla_{\Theta^1} \hat{\mathcal{L}}^1(\Theta^1) + (1 - \alpha) \nabla_{\Theta^1} \hat{\mathcal{L}}^2(\Theta^1, \Theta^2))$;
- 6 $\Theta^2 = \Theta^2 - \eta \nabla_{\Theta^2} \hat{\mathcal{L}}^2(\Theta^1, \Theta^2)$;
- 7 **end**

4 Experiments

Datasets We conduct experiments on four action recognition datasets, including Kinetics400 (K400) (Carreira and Zisserman 2017), UCF101 (Soomro, Zamir, and Shah 2012), HMDB51 (Kuehne et al. 2011) and Something-Something (SS) V1 (Goyal et al. 2017). In K400, UCF101 and HMDB51, temporal relation is less important than the RGB scene information. Most videos from these datasets can be accurately classified by considering only their RGB scene information. In SS V1, many action categories are symmetrical. Discriminating such actions in videos requires modeling temporal data relationships. Mini-Kinetics (Mini-K) (Xie et al. 2018) is sub-set of K400 with 200 categories. Some ablation studies are experimented on Mini-K for fast exploration.

Implementation Details Unless specified otherwise, our models adopt the following settings: the embedded PWTP module is configured with $T = 8, D = 1$. The convolution $\mathcal{F}_s^{k \times k}(\cdot; \theta)$ is configured with the kernel size of 9×9 , stride $s = 8$ and $C' = 24$ output channels. We jointly train the dynamic appearance learning and action recognition tasks with the Multiple Gradient Descent Algorithm described in Sec. 3.4. For SS V1, UCF101 and HMDB51, we use the sparse sampling strategy in TSN (Wang et al. 2016), where a video is evenly divided into S segments. For each segment, we select T consecutive video frames to form a clip of $S \times T$ frames. For K400 (Carreira and Zisserman 2017), we perform dense sampling, selecting $S \times T$ consecutive frames. The dynamic appearance extraction is performed on every T consecutive frames. The training and inference protocols are provided in Appendix A from the SM.

4.1 Main Results

In the following, we present the main results on multiple video benchmarks. To indicate the model that takes dynamic appearance as input, we prefix the model name with DA, and the configuration of $S \times T$ for generating the dynamic appearance is provided as a subscript beside “DA” (*i.e.* $DA_{S \times T}$).

Results on Something-Something Table 1 summarizes a comprehensive comparison, including the inference protocols, corresponding computational costs (FLOPs) and the

prediction accuracy. Our method surpasses the listed methods by good margins. Our DA TSM taking dynamic appearance as input has 1.4% and 10.6% higher top-1 accuracy than TSM R50 taking RGB frame as input and TSM R50 taking optical flow as input, respectively. Moreover, our DA TSM achieves similar accuracy (50.1% *vs.* 50.6%) to the ensemble model of TSM which fuses the predictions of the RGB frame and optical flow modalities. However, the computation of our DA TSM is nearly half of TSM_{RGB+Flow}, when the computation of its optical flow estimation has not been included. The ViT-B (Dosovitskiy et al. 2021) with some small modifications described in Sec. 3.3 provides 45.7% top-1 accuracy, which is lower than most listed models. We give the reason that SS V1 requires models with strong temporal relation reasoning abilities, but the modified ViT-B does not model the interactions between different frames in its attention blocks. Nevertheless, our DA still contributes some improvement to ViT-B (+0.7%). Our DA X3D-XS with X3D-XS backbone produces a similar accuracy as NL I3D (Zhou et al. 2018), but requires 210 times fewer FLOPs per spacetime ‘view’. Meanwhile, DA X3D-XS also produces higher top-1 accuracy (+2.5%) than X3D-XS. By adopting X3D-M as the backbone, our DA X3D-M achieves 53.7% top-1 accuracy, which is 1.7% higher than X3D-M and 1.4% higher than TEA (Li et al. 2020).

Results on K400, UCF101 and HMDB51 Table 2 shows the results on K400, where we list the models with the spatial input size smaller than 256². DA X3D-M achieves 77.3% top-1 accuracy, which is better than X3D-M by 1.3% and better than I3D (Carreira and Zisserman 2017) by a margin of +6.2%. The video-adapted ViT-B (Dosovitskiy et al. 2021) has 76.5% top-1 accuracy which is 1.5% and 2.1% lower than the ViT-based architectures TimeSformer (Bertasius, Wang, and Torresani 2021) and ViT-B-VTN (Neimark et al. 2021), respectively. After taking the dynamic appearance as input, we improve the accuracy of ViT-B to 78.2% (1.7%), which is on par with other Transformer-based models. It is worth mentioning that our improvement in the Transformer backbone is higher than that in the CNN backbones. Although the scene information on K400 is widely considered to be important when distinguishing some actions, the improvement caused by filtering out the static appearance suggests that static features that do not change from frame to frame may impede the enhanced feature learning abilities in standard networks.

The results on UCF101 (Soomro, Zamir, and Shah 2012) and HMDB51 (Kuehne et al. 2011) are shown in Table 3, where we report the mean class accuracy over the three official splits. The recognition accuracy is already saturated on these relatively small-scale datasets. In order to avoid overfitting, we pretrain our model on Kinetics. We consider the inference protocol (3 crops \times 2 clips) for accuracy. DA TSM outperforms most other methods without employing tricks such as multi-stream fusion.

4.2 Ablation Studies

To investigate more configurations we employ the smaller X3D-XS (Feichtenhofer 2020) as the backbone network pro-

Method	Modality	pretrain	Backbone	Frames ×views	FLOPs	#Param.	Top-1 (%)	Top-5 (%)
TRN (Zhou et al. 2018)	RGB	RGB+Flow	IN-1K	BNInc.	$(8+40) \times 1$	N/A	36.6M	42.0
ir-CSN (Tran et al. 2019)		None	3D R152	32×10	$74G \times 10$	29.7M	49.3	-
NL I3D (Wang et al. 2018b)		K400	3D R50	32×2	$168G \times 2$	N/A	44.4	76.0
TEA (Li et al. 2020)		IN-1K	R50	16×30	$70G \times 30$	24.4M	52.3	81.9
TDN (Wang et al. 2021)			R101	16×1		$132G \times 1$	55.3	83.3
ViT-B \dagger (Dosovitskiy et al. 2021)	RGB	IN-21K	-	8×3	$269G \times 3$	86.3M	45.7	74.3
ViT-B\dagger (Ours)		$DA_{S=8,T=4}$	-	8×3	$270G \times 3$	86.3M	46.4	75.8
TSM (Lin, Gan, and Han 2019)	RGB	Flow	IN-1K	8×6	$42.9G \times 6$	23.8M	48.7	77.9
TSM (Lin, Gan, and Han 2019)		RGB+Flow		40×6	N/A	48.6M	39.5	70.5
TSM (Lin, Gan, and Han 2019)		$DA_{S=8,T=4}$		$(8+40) \times 3$	N/A	48.6M	50.6	80.1
TSM (ours)				8×6	$43.1G \times 6$	23.8M	50.1	78.6
X3D-XS (Feichtenhofer 2020)	RGB	$DA_{S=4,T=8}$	K400	-	$0.6G \times 6$	3.33M	40.6	70.5
X3D-XS (ours)		-		4×6	$0.8G \times 6$	3.34M	43.1	73.4
X3D-M (Feichtenhofer 2020)		$DA_{S=16,T=3}$		-	16×6	$6.3G \times 6$	3.33M	52.0
X3D-M (ours)				-	16×6	$7.0G \times 6$	3.34M	53.7
								82.1

Table 1: Results on SS V1. “N/A” indicates the numbers are not available. “Frames” indicates the frames of a given input modality. “views” indicates spatial crops × temporal clips. \dagger denotes our reimplementation.

cessing $S = 4$ segments, unless specified otherwise.

Smaller Projection Error, Higher Classification Accuracy? The criterion of the dynamic appearance learning task $\hat{\mathcal{L}}^1(\Theta^1)$ and the action recognition criterion $\hat{\mathcal{L}}^2(\Theta^1, \Theta^2)$ are supposed to be positive within a certain range, but this is not always true. To find out the correlation of $\hat{\mathcal{L}}^1$ and $\hat{\mathcal{L}}^2$ we optimize the model with only $\hat{\mathcal{L}}^2$ and record the changes for $\hat{\mathcal{L}}^1$ and $\hat{\mathcal{L}}^2$ in different training periods. From the plots in Fig. 3(a) and (b) on UCF101 and Mini-Kinetics, respectively, we observe that $\hat{\mathcal{L}}^1$ and $\hat{\mathcal{L}}^2$ show positive correlation within the chosen range. The positive correlation indicates that it is feasible to set the projection task $\hat{\mathcal{L}}^1(\Theta^1)$ of PWTP as an auxiliary task helping the model to generalize better on the action recognition task $\hat{\mathcal{L}}^2(\Theta^1, \Theta^2)$. Outside of the specific range, we may obtain negative correlation, given the evidence from Table 5, where separate training causes $\hat{\mathcal{L}}^1$ to over-focus on the auxiliary task, resulting in a performance drop on the primary recognition task. When optimizing the PWTP module independently, a too small $\hat{\mathcal{L}}^1$ could result in PWTP summarizing both static and dynamic appearance information into the same subspace. Meanwhile, the projection residual \mathbf{p} would carry very little information, failing to represent abundant dynamic appearances. To tackle this issue, we set $D \ll T$, as stated in Sec. 3.1.

Joint training The dynamic appearance learning task and action recognition task could either be optimized separately or through joint training. In Table 5 we investigate the effect of separate training and different joint training approaches on performance. In summary, joint training approaches have higher accuracy than the separate training strategy. We note that the joint training with MGDA (Désidéri 2012) produces higher accuracy than the fixed scale strategy, which demonstrate the effectiveness of MGDA. We have also explored

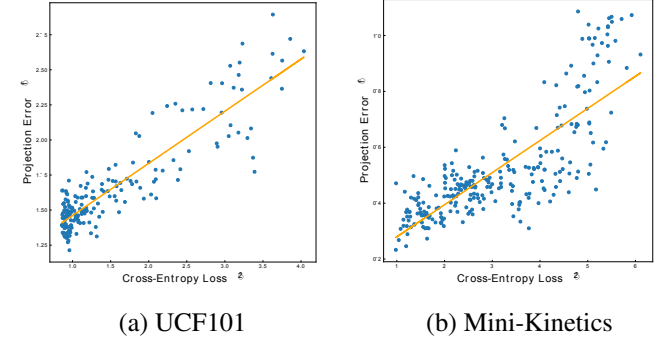


Figure 3: Example scatterplots of variables $\hat{\mathcal{L}}^1$ and $\hat{\mathcal{L}}^2$ on dataset (a) UCF101 and (b) Mini-Kinetics

some other joint training approaches, the details of which are provided in the Appendix D from the SM.

Instantiations and Settings of PWTP We consider various configurations of PWTP on SS V1 and Mini-Kinetics, vary T and D from Eq. (4) and evaluate the recognition accuracy. Table 4b shows that the configurations with $T = 8$ have higher accuracy than $T = 4$ but lower accuracy than $T = 16$, which suggests that longer frame sequences can help PWTP to capture a diversity of dynamic appearances regarding movement and generate better results. When fixing $T = 8$, the setting of $D = 3$ is better than that of $D = 1$, which suggests that a relatively larger D endues PWTP with stronger information summarization capacity and helps generate lower ENoPR and higher accuracy. Nevertheless, D should not set to be larger than half of T , as we have seen a performance drop when setting $D > \frac{1}{2}T$ in our preliminary experiments.

The spatial convolution $\mathcal{F}_s^{k \times k}(\cdot; \theta)$ from Eq. (2) is used for local information aggregation. We ablate various settings

Method	pretrain	Frames × views	FLOPs	Top1 (%)	Top5 (%)
SlowFast _{4×16} (Feichtenhofer et al. 2019)		32×30	1083G	75.6	92.1
ip-CSN (Tran et al. 2019)		32×30	2490G	76.8	92.5
I3D _{RGB} (Carreira and Zisserman 2017)	IN-1K	64×N/A	N/A	71.1	89.3
NL I3D (Wang et al. 2018b)		128×30	10770G	77.7	93.3
MViT-B _{16×4} (Fan et al. 2021)		16×5	352G	78.4	93.5
TimeSformer (Bertasius, Wang, and Torresani 2021)	IN-21K	8×3	590G	78.0	93.7
ViT-B-VTN (Neimark et al. 2021)		250×1	4218G	78.6	93.7
TSM R50 (Lin, Gan, and Han 2019)	IN-1K	16×30	2577G	74.7	-
DA_{16×8} TSM		16×30	2602G	75.9	92.2
X3D-M (Feichtenhofer 2020)	None	16×30	191G	76.0	92.3
DA_{16×8}X3D-M		16×30	216G	77.3	92.8
ViT-B \dagger (Dosovitskiy et al. 2021)	IN-21K	8×3	808G	76.5	92.6
DA_{8×8}ViT-B\dagger		8×3	809G	78.2	93.4

Table 2: Results on K400. We report the inference cost of multiple “views” (spatial crops × temporal clips). \dagger denotes our reimplementation.

Method	HMDB	UCF
StNet (He et al. 2019)	-	93.5
TSM (Lin, Gan, and Han 2019)	73.5	95.9
STM (Jiang et al. 2019)	72.2	96.2
TEA (Li et al. 2020)	73.3	96.9
Four-Stream (Bilen et al. 2018)	72.5	95.5
TVNet (Fan et al. 2018)	71.0	94.5
TSN _{RGB+Flow} (Wang et al. 2016)	68.5	94.0
OFF _{RGB+Flow} (Sun et al. 2018)	74.2	96.0
DA_{8×16}TSM	75.3	96.5

Table 3: Results on HMDB51 and UCF101. We report the mean class accuracy (%) over the three official splits.

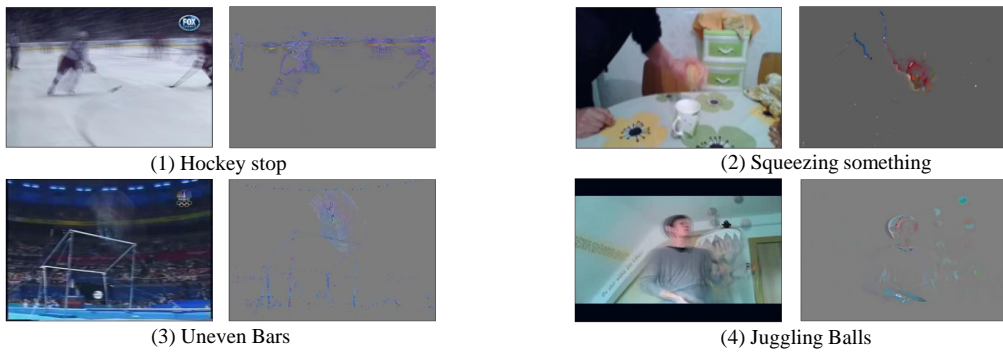


Figure 4: Example video sequences visualized as their frame averaging (left) and corresponding dynamic appearances (right). The videos are randomly picked from the four datasets.

Stride s	Kernel size $k \times k$	#Channels C'	Mini-K		SS V1		FLOPs	T	D	Mini-K		SS V1		FLOPs
			ENoPR	Acc.	ENoPR	Acc.				ENoPR	Acc.	ENoPR	Acc.	
1	7×7	12	0.26	55.1	0.14	40.9	2.60G	4	1	0.26	56.2	0.16	39.3	0.71G
1	7×7	24	0.22	58.6	0.13	41.1	4.06G	4	2	0.24	55.3	0.08	39.5	0.71G
4	7×7	24	0.32	58.1	0.18	41.3	0.95G	8	1	0.41	56.9	0.27	41.0	0.82G
8	9×9	24	0.41	56.9	0.27	41.0	0.82G	8	3	0.33	57.0	0.13	41.3	0.83G
8	11×11	24	0.37	57.1	0.20	41.2	0.86G	16	1	0.72	58.6	0.39	42.1	1.12G

(a) Evaluating various settings of convolution $\mathcal{F}_s^{k \times k}$ in the PWTP module

(b) Evaluating PWTP when changing D and T

Table 4: Ablation Studies for PWTP on Something-Something (SS) V1 and Mini-Kinetics (Mini-K). The computational cost (FLOPs) of X3D-XS with a PWTP module embedded is reported.

of $\mathcal{F}_s^{k \times k}(\cdot; \theta)$, including changing the stride s , kernel size $k \times k$, output channel number C' and the results are provided in Table 4a. A larger kernel of $\mathcal{F}_s^{k \times k}(\cdot; \theta)$ can receive information from a larger local region, and therefore PWTP can encode additional spatial information into the temporal descriptor \mathbf{u} , which helps the model to produce higher accuracy. In addition, Table 4a shows that a large stride s for the

convolution $\mathcal{F}_s^{k \times k}(\cdot; \theta)$ can significantly reduce the computational cost while maintaining performance.

Efficiency and Effectiveness of the Dynamic Appearance

We draw an apple-to-apple comparison between the proposed dynamic appearance and other motion representations (Bilen et al. 2018; Fan et al. 2018; Ilg et al. 2017; Zach, Pock, and Bischof 2007). The comparison results are

Joint Training Approach	ENoPR ($\hat{\mathcal{L}}^1$)	Acc. (%)
Baseline	-	38.3
Separate training	0.17	39.4
Constant Scale ($\alpha = 0$)	0.43	39.2
Constant Scale ($\alpha = 0.5$)	0.34	40.1
Constant Scale ($\alpha = 0.9$)	0.22	39.3
MGDA	0.27	41.0

Table 5: Results for different joint training approaches on SS V1. The baseline is the network with RGB frame input.

Representation Method	Efficiency Metrics		SS V1	UCF101
	FLOPs	#Param.		
RGB (baseline)	-	-	46.5	87.1
Flow	-	-	37.4	88.5
RGB+Flow	-	-	49.8	93.9
RGB Diff (Wang et al. 2016)	-	-	46.6	87.0
Dynamic Image \dagger (Bilen et al. 2018)	-	-	43.3	86.2
FlowNetC \dagger (Ilg et al. 2017)	444G	39.2M	26.3	87.3
FlowNetS \dagger (Ilg et al. 2017)	356G	38.7M	23.4	86.8
TVNet \dagger (Fan et al. 2018)	3.30G	0.20K	45.2	88.6
DA	0.23G	7.13K	48.7	89.7

Table 6: DA vs. other motion representation methods. \dagger denotes our reimplementation. The additional parameters and computation (FLOPs) required by the representation methods are reported.

shown in Table 6. For all the video representation methods, we guarantee they consume the same number of raw video frames (48 frames). More details can be found in Appendix B from the SM. The motion representations produced by these methods are used as inputs to TSM R50 (Lin, Gan, and Han 2019). The prediction scores are obtained by the average consensus of eight temporal segments (Wang et al. 2016). The network that takes the proposed dynamic appearance as input outperforms all other motion representation methods by big margins within reasonable computational costs. In SS V1, our method achieves similar accuracy to the fusion of “RGB+Flow”.

4.3 Visualization analysis

Visualization results of dynamic appearances are provided in Fig. 4. the example dynamic appearance suppresses the background movement and stationary information and retains the appearance information characteristic to motion. In Fig. 5 we compare dynamic appearances with TV-L1 Flow (Zach, Pock, and Bischof 2007) and TVNet (Fan et al. 2018). TV-L1 Flow and TVNet represent motion with instantaneous image velocities, losing the color and appearance information related to moving objects. However, the dynamic appearances preserved the essential parts of moving objects’ visual information, which is vital for discriminating different actions. In Fig. 6, we compare visually the Dynamic Appearance and Dynamic Image (Bilen et al. 2018). The dynamic image results in poor discrimination be-

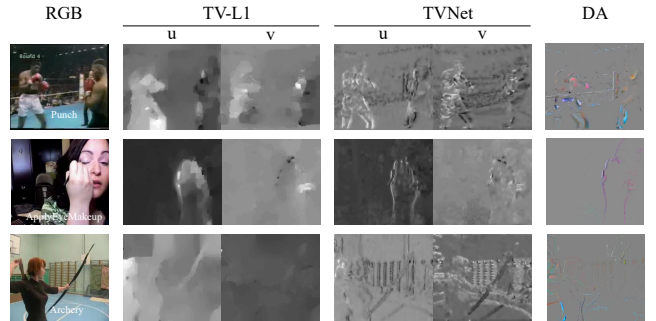


Figure 5: Visual examples of different video representations. Best viewed in color and zoomed in.

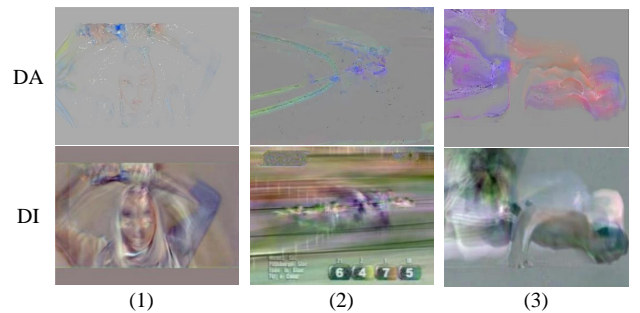


Figure 6: Visualization of Dynamic Appearance (DA) and Dynamic Image (DI).

tween the moving objects and background when we have camera shaking or movement, as we can observe from Fig. 6(2). On the contrary, the dynamic appearance is robust to camera movement, clearly representing the visual information related to motion. More visualization examples are provided in Appendix E, where we show that Dynamic Appearance steadily works on a wide range of actions.

5 Conclusion

We have proposed the Pixel-Wise Temporal Projection (PWTP), a lightweight and backbone-agnostic module, which achieves the disentanglement of video static and dynamic appearance. The extracted dynamic appearance (DA) characterizes movement by summarizing the visual appearance information that changes from frame to frame. We integrate the PWTP module with a CNN or Visual Transformer (ViT) into an efficient and effective spatio-temporal architecture, set in an end-to-end trainable framework. The multiple gradient descent algorithm is used for the joint training of PWTP and the deep network. With extensive experimental results on multiple challenging video benchmarks, we have demonstrated that the proposed dynamic appearances are a qualified input resource to deep networks, showing great advantages over RGB frames and the optical flow inputs, in terms of efficiency and effectiveness. The proposed video representation methodology can contribute to designing optimal spatio-temporal video modeling systems.

References

- Ahad, M.; Ogata, T.; Tan, J.; Kim, H.; and Ishikawa, S. 2008. Motion recognition approach to solve overwriting in complex actions. In *International Conference on Automatic Face & Gesture Recognition*, 1–6. IEEE.
- Arnab, A.; Dehghani, M.; Heigold, G.; Sun, C.; Lučić, M.; and Schmid, C. 2021. Vivit: A video vision transformer. In *Proc. IEEE Int. Conference Computer Vision (ICCV)*, 6836–6846.
- Bertasius, G.; Wang, H.; and Torresani, L. 2021. Is space-time attention all you need for video understanding. In *Proc. Int. Conference Mach. Learn. (ICML)*.
- Bilen, H.; Fernando, B.; Gavves, E.; and Vedaldi, A. 2018. Action recognition with dynamic image networks. *IEEE Trans. on Pattern Analysis and Machine Intelligence*, 40(12): 2799–2813.
- Bradski, G.; and Davis, J. 2002. Motion segmentation and pose recognition with motion history gradients. *Machine Vision and Applications*, 13(3): 174–184.
- Carreira, J.; and Zisserman, A. 2017. Quo vadis, action recognition? a new model and the kinetics dataset. In *Proc. IEEE Conference Computer Vision Pattern Recog. (CVPR)*, 4724–4733.
- Deng, J.; Dong, W.; Socher, R.; Li, L.-J.; Li, K.; and Fei-Fei, L. 2009. Imagenet: A large-scale hierarchical image database. In *Proc. IEEE Conference Computer Vision Pattern Recog. (CVPR)*, 248–255.
- Désidéri, J. 2012. Multiple-gradient descent algorithm (MGDA) for multiobjective optimization. *Comptes Rendus Mathematique*, 350(5-6): 313–318.
- Dosovitskiy, A.; Beyer, L.; Kolesnikov, A.; Weissenborn, D.; Zhai, X.; Unterthiner, T.; Dehghani, M.; Minderer, M.; Heigold, G.; Gelly, S.; et al. 2021. An image is worth 16x16 words: Transformers for image recognition at scale. *Int. Conf. Learn. Represent. (ICLR)*, *arXiv preprint arXiv:2010.11929*.
- Dosovitskiy, A.; Fischer, P.; Ilg, E.; Hausser, P.; Hazirbas, C.; Golkov, V.; Van Der Smagt, P.; Cremers, D.; and Brox, T. 2015. Flownet: Learning optical flow with convolutional networks. In *Proc. IEEE Int. Conference Computer Vision (ICCV)*, 2758–2766.
- Fan, H.; Xiong, B.; Mangalam, K.; Li, Y.; Yan, Z.; Malik, J.; and Feichtenhofer, C. 2021. Multiscale vision transformers. In *Proc. IEEE Int. Conference Computer Vision (ICCV)*, 6824–6835.
- Fan, L.; Huang, W.; Gan, C.; Ermon, S.; Gong, B.; and Huang, J. 2018. End-to-end learning of motion representation for video understanding. In *Proc. IEEE Conference Computer Vision Pattern Recog. (CVPR)*, 6016–6025.
- Feichtenhofer, C. 2020. X3D: Expanding Architectures for Efficient Video Recognition. In *Proc. IEEE Conf. Computer Vision and Pattern Recognition (CVPR)*, 203–213.
- Feichtenhofer, C.; Fan, H.; Malik, J.; and He, K. 2019. Slow-fast networks for video recognition. In *Proc. IEEE Int. Conf. on Computer Vision (ICCV)*, 6202–6211.
- Feichtenhofer, C.; Pinz, A.; and Wildes, R. 2016. Spatiotemporal residual networks for video action recognition. In *Advances in Neural Information Processing Systems (NIPS)*, 3468–3476.
- Feichtenhofer, C.; Pinz, A.; and Zisserman, A. 2016. Convolutional two-stream network fusion for video action recognition. In *Proc. IEEE Conference Computer Vision Pattern Recog. (CVPR)*, 1933–1941.
- Fernando, B.; Gavves, E.; Oramas, J. M.; Ghodrati, A.; and Tuytelaars, T. 2015. Modeling video evolution for action recognition. In *Proc. IEEE Conference Computer Vision Pattern Recog. (CVPR)*, 5378–5387.
- Goyal, R.; Kahou, S. E.; Michalski, V.; Materzynska, J.; Westphal, S.; Kim, H.; Haenel, V.; Fruend, I.; Yianilos, P.; Mueller-Freitag, M.; et al. 2017. The “Something Something” Video Database for Learning and Evaluating Visual Common Sense. In *Proc. IEEE Int. Conf. on Computer Vision (ICCV)*, volume 1, 5842–5850.
- Hara, K.; Kataoka, H.; and Satoh, Y. 2018. Can spatiotemporal 3d cnns retrace the history of 2d cnns and imagenet? In *Proc. IEEE Conference Computer Vision Pattern Recog. (CVPR)*, 6546–6555.
- He, D.; Zhou, Z.; Gan, C.; Li, F.; Liu, X.; Li, Y.; Wang, L.; and Wen, S. 2019. Stnet: Local and global spatial-temporal modeling for action recognition. In *Proc. AAAI Conference on Artif. Intel.*, volume 33, 8401–8408.
- He, K.; Zhang, X.; Ren, S.; and Sun, J. 2016. Deep residual learning for image recognition. In *Proc. IEEE Conference Computer Vision Pattern Recog. (CVPR)*, 770–778.
- Ilg, E.; Mayer, N.; Saikia, T.; Keuper, M.; Dosovitskiy, A.; and Brox, T. 2017. Flownet 2.0: Evolution of optical flow estimation with deep networks. In *Proc. IEEE Conference Computer Vision Pattern Recog. (CVPR)*, volume 2, 2462–2470.
- Ioffe, S.; and Szegedy, C. 2015. Batch Normalization: Accelerating Deep Network Training by Reducing Internal Covariate Shift. In *Proc. Int. Conference Mach. Learn. (ICML)*, vol. *PMLR 37*, 448–456.
- Jiang, B.; Wang, M.; Gan, W.; Wu, W.; and Yan, J. 2019. Stmt: Spatiotemporal and motion encoding for action recognition. In *Proc. IEEE Int. Conference Computer Vision (ICCV)*, 2000–2009.
- Karpathy, A.; Toderici, G.; Shetty, S.; Leung, T.; Sukthankar, R.; and Fei-Fei, L. 2014. Large-scale video classification with convolutional neural networks. In *Proc. IEEE Conference Computer Vision Pattern Recog. (CVPR)*, 1725–1732.
- Krizhevsky, A.; Sutskever, I.; and Hinton, G. 2012. Imagenet classification with deep convolutional neural networks. In *Advances Neural Information Process. Systems (NIPS)*, 1097–1105.
- Kuehne, H.; Jhuang, H.; Garrote, E.; Poggio, T.; and Serre, T. 2011. HMDB: a large video database for human motion recognition. In *Proc. IEEE Int. Conference Computer Vision (ICCV)*, 2556–2563.

- Li, Y.; Ji, B.; Shi, X.; Zhang, J.; Kang, B.; and Wang, L. 2020. TEA: Temporal Excitation and Aggregation for Action Recognition. In *Proc. IEEE Conference Computer Vision Pattern Recog. (CVPR)*, 909–918.
- Lin, J.; Gan, C.; and Han, S. 2019. Tsm: Temporal shift module for efficient video understanding. In *Proc. IEEE Int. Conference Computer Vision (ICCV)*, 7083–7093.
- Loshchilov, I.; and Hutter, F. 2017. SGDR: Stochastic gradient descent with warm restarts. *Int. Conf. Learn. Represent. (ICLR)*, *arXiv preprint arXiv:1608.03983*.
- Loshchilov, I.; and Hutter, F. 2019. Decoupled Weight Decay Regularization. In *Int. Conf. Learn. Represent. (ICLR)*, *arXiv preprint arXiv:1711.05101*.
- Neimark, D.; Bar, O.; Zohar, M.; and Asselmann, D. 2021. Video transformer network. In *Proc. IEEE Int. Conference Computer Vision (ICCV)*, 3163–3172.
- Ng, J. Y.-H.; Choi, J.; Neumann, J.; and Davis, L. S. 2018. Actionflownet: Learning motion representation for action recognition. In *2018 IEEE Winter Conference on Applications of Computer Vision (WACV)*, 1616–1624. IEEE.
- Piergiovanni, A.; and Ryoo, S. 2019. Representation flow for action recognition. In *Proc. IEEE Conference Computer Vision Pattern Recog. (CVPR)*, 9945–9953.
- Qiu, Z.; Yao, T.; and Mei, T. 2017. Learning spatio-temporal representation with pseudo-3d residual networks. In *Proc. IEEE Int. Conference Computer Vision (ICCV)*, 5533–5541.
- Sener, O.; and Koltun, V. 2018. Multi-Task Learning as Multi-Objective Optimization. In *Advances Neural Information Process. Systems (NIPS)*, 525–536.
- Simonyan, K.; and Zisserman, A. 2014. Two-stream convolutional networks for action recognition in videos. In *Advances Neural Information Process. Systems (NIPS)*, 568–576.
- Simonyan, K.; and Zisserman, A. 2015. Very Deep Convolutional Networks for Large-Scale Image Recognition. In *Int. Conf. Learn. Represent. (ICLR)*, *arXiv preprint arXiv:1409.1556*.
- Soomro, K.; Zamir, A. R.; and Shah, M. 2012. UCF101: A dataset of 101 human actions classes from videos in the wild. *arXiv preprint arXiv:1212.0402*.
- Sun, D.; Vlasic, D.; Herrmann, C.; Jampani, V.; Krainin, M.; Chang, H.; Zabih, R.; Freeman, W.; and Liu, C. 2021. Autoflow: Learning a better training set for optical flow. In *Proceedings of the IEEE/CVF Conference on Computer Vision and Pattern Recognition (CVPR)*, 10093–10102.
- Sun, S.; Kuang, Z.; Sheng, L.; Ouyang, W.; and Zhang, W. 2018. Optical flow guided feature: A fast and robust motion representation for video action recognition. In *Proc. IEEE Conference Computer Vision Pattern Recog. (CVPR)*, 1390–1399.
- Szegedy, C.; Liu, W.; Jia, Y.; Sermanet, P.; Reed, S.; Anguelov, D.; Erhan, D.; Vanhoucke, V.; and Rabinovich, A. 2015. Going deeper with convolutions. In *Proc. IEEE Conference Computer Vision Pattern Recog. (CVPR)*, 1–9.
- Szegedy, C.; Vanhoucke, V.; Ioffe, S.; Shlens, J.; and Wojna, Z. 2016. Rethinking the inception architecture for Comp. vision. In *Proc. IEEE Conference Computer Vision Pattern Recog. (CVPR)*, 2818–2826.
- Taylor, G. W.; Fergus, R.; LeCun, Y.; and Bregler, C. 2010. Convolutional learning of spatio-temporal features. In *Proc. European Conference Computer Vision (ECCV)*, 140–153.
- Tran, D.; Bourdev, L.; Fergus, R.; Torresani, L.; and Paluri, M. 2015. Learning spatiotemporal features with 3D convolutional networks. In *Proc. IEEE Int. Conference Computer Vision (ICCV)*, 4489–4497.
- Tran, D.; Wang, H.; Torresani, L.; and Feiszli, M. 2019. Video classification with channel-separated convolutional networks. In *Proc. IEEE Int. Conference Computer Vision (ICCV)*, 5552–5561.
- Tran, D.; Wang, H.; Torresani, L.; Ray, J.; LeCun, Y.; and Paluri, M. 2018. A closer look at spatiotemporal convolutions for action recognition. In *Proc. IEEE Conference Computer Vision Pattern Recog. (CVPR)*, 6450–6459.
- Wang, J.; Cherian, A.; Porikli, F.; and Gould, S. 2018a. Video representation learning using discriminative pooling. In *Proc. IEEE Conference Computer Vision Pattern Recog. (CVPR)*, 1149–1158.
- Wang, L.; Tong, Z.; Ji, B.; and Wu, G. 2021. Tdn: Temporal difference networks for efficient action recognition. In *Proc. IEEE Conference Computer Vision Pattern Recog. (CVPR)*, 1895–1904.
- Wang, L.; Xiong, Y.; Wang, Z.; Qiao, Y.; Lin, D.; Tang, X.; and Van Gool, L. 2016. Temporal segment networks: Towards good practices for deep action recognition. In *Proc. European Conference Computer Vision (ECCV)*, vol. *LNCS 9912*, 20–36.
- Wang, X.; Girshick, R.; Gupta, A.; and He, K. 2018b. Non-local neural networks. In *Proc. IEEE Conference Computer Vision Pattern Recog. (CVPR)*, 7794–7803.
- Wang, Y.; Long, M.; Wang, J.; and Yu, P. 2017. Spatiotemporal pyramid network for video action recognition. In *Proc. IEEE Conference Computer Vision Pattern Recog. (CVPR)*, 1529–1538.
- Xie, S.; Sun, C.; Huang, J.; Tu, Z.; and Murphy, K. 2018. Rethinking spatiotemporal feature learning: Speed-accuracy trade-offs in video classification. In *Proc. European Conference Computer Vision (ECCV)*, vol. *LNCS 11219*, 305–321.
- Yue-Hei Ng, J.; Hausknecht, M.; Vijayanarasimhan, S.; Vinyals, O.; Monga, R.; and Toderici, G. 2015. Beyond short snippets: Deep networks for video classification. In *Proc. IEEE Conference Computer Vision Pattern Recog. (CVPR)*, 4694–4702.
- Zach, C.; Pock, T.; and Bischof, H. 2007. A duality based approach for realtime TV-L1 optical flow. In *Proc. Joint Pattern Recog. Symp.*, vol. *LNCS 4713*, 214–223.
- Zhou, B.; Andonian, A.; Oliva, A.; and Torralba, A. 2018. Temporal relational reasoning in videos. In *Proc. European Conference Computer Vision (ECCV)*, 803–818.
- Zhu, Y.; Lan, Z.; Newsam, S.; and Hauptmann, A. 2018. Hidden two-stream convolutional networks for action recognition. In *Asian Conference on Computer Vision*, 363–378. Springer.

A Additional Implementation details

In the following we provide additional implementation details and parameter settings in our models. We train our models using synchronized SGD with momentum 0.9 and a cosine learning rate schedule. By default, we add a dropout layer before the classification layer in our models to prevent overfitting. To avoid over-fitting, we apply L2 regularization to the convolutional and classification layers. Meanwhile, we use label-smoothing (Szegedy et al. 2016) of 0.1 and gradient clip of 20. Following the experimental settings in (Lin, Gan, and Han 2019; Wang et al. 2016), the learning rate and weight decay parameters for the classification layers are 5 times larger than those for the convolutional layers. Besides, when training on Something-Something V1, we do not apply random horizontal flip to the training data.

For efficient inference, we sample a single clip per video with center cropping used in the ablation studies. The spatial size of a center crop is of 160×160 for the models with X3D-XS backbone, while for the others is 224×224 . When pursuing high accuracy, we sample multiple clips&crobs from the video and average the softmax scores of multiple spacetime “views” (spatial crops \times temporal clips) for prediction. Following the practice in (Feichtenhofer et al. 2019), we approximate the fully-convolutional testing by taking 3 crops of 256×256 pixels (160×160 for X3D-XS) to cover the spatial dimensions.

Hyperparameters for the model based on ResNet The backbone networks are pretrained on ImageNet-1K (Deng et al. 2009). On Kinetics400, we train our models on 64 GPUs (NVIDIA Tesla V100). The initial learning rate, batch size, total epochs, weight decay and dropout ratio are set to 0.08, 512 (8 samples per GPU), 100, 2e-4 and 0.5, respectively. On Something-Something V1, we train our models in 32 GPUs, and the hyperparameters mentioned above are set to 0.12, 256 (8 samples per GPU), 50, 8e-4 and 0.8, respectively. We use linear warm-up (Loshchilov and Hutter 2017) for the first 7 epochs to overcome early optimization difficulty. When fine-tuning the Kinetics models on UCF101 and HMDB51, we train our models on 16 GPUs and freeze the entire batch normalization (Ioffe and Szegedy 2015) layers except for the first one to avoid overfitting, following the recipe in (Wang et al. 2016). The initial learning rate, batch size, total epochs, weight decay and dropout ratio are set to 0.001, 64 (4 samples per GPU), 10, 1e-4 and 0.8, respectively.

Hyperparameters for the model based on X3D On Kinetics400, we train our models on 32 GPUs. The initial learning rate, batch size, total epochs, weight decay and dropout ratio are set to 0.4, 256 (8 samples per GPU), 256, 5e-5 and 0.5, respectively. On Something-Something V1, the backbone networks are pretrained on Kinetics. We train our models on 32 GPUs, and these hyperparameters are set to 0.12, 256 (8 samples per GPU), 50, 4e-4 and 0.8, respectively.

Hyperparameters for the model based on ViT The backbone networks are pretrained on ImageNet-21K (Deng et al. 2009). In the training of ViT-based models, we do not

use drop out, gradient clip and label-smoothing. The initial learning rate, batch size, total epochs, weight decay are set to 0.004, 64 (2 samples per GPU), 15, 1e-4, respectively. The learning rate for the PWTP module is 5 times larger than those for layers in ViT.

B Implementation details of Efficiency and Effectiveness of Dynamic Appearance

These additional explanations are helpful for Section 4.2.4 from page 7-8 of the main paper. In order to fairly evaluate different video representation methods (Bilen et al. 2018; Fan et al. 2018; Ilg et al. 2017; Zach, Pock, and Bischof 2007), we reimplement these methods in the same experimental settings with the code provided by the original authors. In our reimplementation, Dynamic Image method generate one frame of representation for every 6 video frames, which is the same as our method. As for TVNet and TV-L1 Flow, we stack 5 frames of the estimated flow along the channel dimension to form an input frame with 10 channels, in total processing 6 RGB frames in a segment. All the models are pretrained on ImageNet-1K and then trained with the same hyperparameters.

In order to assess whether the performance gain of models that take dynamic appearances as inputs is or not due to the additional FLOPs and parameters, we compare our DA model with those models that have higher computational costs than ours. From the results shown in Fig. 7, we can observe that our TSM R50 that takes dynamic appearances as input has even higher accuracy than TSM R101 (48.7% vs. 46.9%) on Something-Something, but the FLOPs and the number of parameters are much less than TSM R101, which demonstrate the performance gain of our model is more due to the efficient motion modeling in dynamic appearances.

C Design of Multilayer Perceptron (MLP)

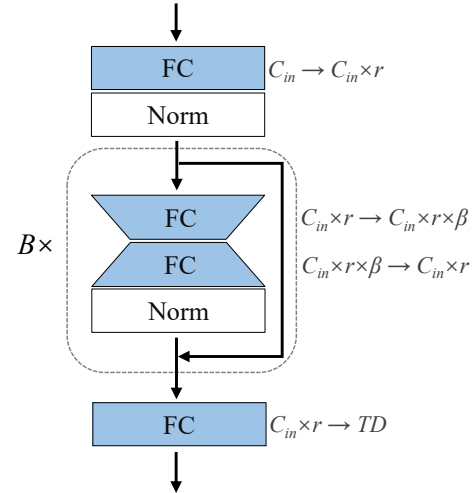


Figure 7: The scheme of MLP in the PWTP module

The MLP in the PWTP module is used to generate the input-specific hyperplanes \mathbf{A} in Equation (4) from Section

Model	Efficiency Metrics		SS V1	UCF101
	FLOPs	#Param.		
TSM R50 (Lin, Gan, and Han 2019)	42.9G	23.8 M	46.5	87.1
TSM R50+Conv	44.5G	23.8M+2.6K	46.3	87.0
TSM R101 (Lin, Gan, and Han 2019)	62.5G	42.8 M	46.9	-
DA TSM R50	43.1G	23.8M+7.13K	48.7	89.7

Table 7: Comparisons with heavier models on Something-Something (SS) V1 and UCF101

3.1, page 5 of the main paper. In Figure 7, we present the scheme of the MLP, where the feature numbers of the fully-connected (FC) layers are specified on their right side. The first FC expends the number of features with a factor of r . The MLP contains B bottleneck blocks. Each bottleneck block comprises a normalization layer and two FC layers, where the number of features is first reduced by a factor of β and then recovered to its original size. For the normalization, we use Batch Normalization, which behaves more stably than Layer Normalization in our study. In Equation (4) from the main paper, the number of input channels for the MLP is $C_{in} = \frac{T \times (T-1)}{2}$, while the number of output channels is TD . Here, we treat PWTP as an individual optimization problem and evaluate its representation capacity by ENoPR $\hat{\mathcal{L}}^1(\Theta^1)$ on Mini-Kinetics. The specifications of the MLP’s various configurations are listed in Table 8, in which the PWTP modules are trained for 10 epochs with AdamW optimizer (Loshchilov and Hutter 2019). We can see that aside from Config #6, which does not use bottleneck blocks, the rest of the configurations have similar ENoPR ($\hat{\mathcal{L}}^1$). To balance the capacity/speed trade-off, we use Config #7 as the default MLP configuration in our experiments.

D Scale Scheduler for Joint Training

When using joint training to resolve the multi-objective optimization problem defined in Equation (9) from the paper, we also consider employing a scale scheduler to produce a dynamic scale α , weighting the contribution of the two components $\hat{\mathcal{L}}^1(\Theta^1)$ and $\hat{\mathcal{L}}^2(\Theta^1, \Theta^2)$. The scale scheduler is a hybrid function that initially sets α to a large value and gradually decreases it to a minimum value, simulating the cosine annealing (Loshchilov and Hutter 2017):

$$\alpha = \begin{cases} \frac{1}{2}(1 + \cos(\pi \log_{[(\gamma M)^{\cos^{-1}(2\lambda-1)}]} m)), & m < \gamma M \\ \frac{1}{2}\lambda(1 + \cos(\pi \log_{[(1-\gamma)M]} m)), & m \geq \gamma M \end{cases} \quad (13)$$

where m denotes the current iteration, M represents the total number of training iterations, while $\gamma \geq 1$ and $\lambda \leq 1$ are two additional parameters used to control the graph of the hybrid function. Some example graphs of the hybrid function are displayed in Figure 8. The scale scheduler is established under the realistic assumption that in the early training period, the feature representation learning task $\hat{\mathcal{L}}^1(\Theta^1)$ has higher priority than the recognition task $\hat{\mathcal{L}}^2(\Theta^1, \Theta^2)$. In the later training period, the primary action recognition task should

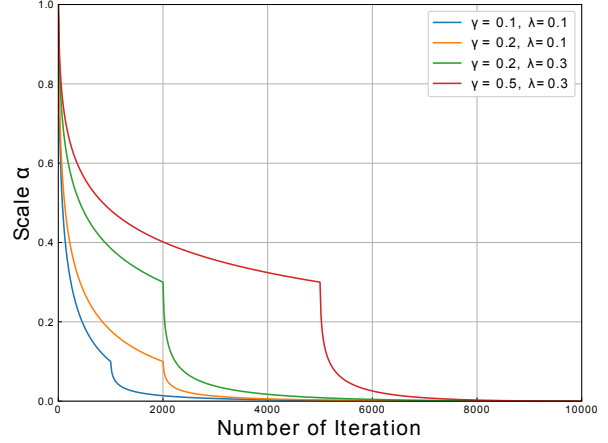


Figure 8: Example graphs of the scale schedule function with different γ and λ

be the main focus, and the optimization objective of the feature representation learning task should be assigned a very low weight. We use the small network X3D-XS (Feichtenhofer 2020) as the backbone network processing $S = 4$ segments. The results of using the scale scheduler are shown in Table 9. The scale scheduler works better than the fixed scale method. Although the scale scheduler introduces two additional parameters λ and γ , its performance is not that sensitive to changes in these parameters, as can be observed from the results in Table 9.

E More visualization analysis results

Dynamic Appearance of longer sequences We attempt to extract the dynamic appearances from video frame sequences of different lengths (T). Some visualization examples are presented in Figure 9. We can observe that the dynamic appearances generated by longer frame sequences contain additional visual information characterizing the movement. According to the results in Table 10, the dynamic appearances extracted from longer frame sequences have higher accuracy. We do not experiment with longer frame sequences on the Something-Something dataset because many videos in that dataset contain fewer than 50 frames, which is not enough to form a valid input when X3D-XS processes $S = 4$ segments.

More dynamic appearance examples We provide more visualization examples in Figures 10 and 11, where we pro-

Config	Bottleneck ratio (β)	Number of blocks (B)	Expansion ratio (r)	ENoPR ($\hat{\mathcal{L}}^1$)	FLOPs	Params
#1	1/4	1	4	0.26	45.3M	16.9k
#2	1/4	1	1	0.27	38.0M	7.4k
#3	1/4	2	1	0.28	38.3M	7.9k
#4	1/4	2	4	0.26	50.2M	23.3k
#5	1	1	4	0.28	59.8M	35.5k
#6	1/4	0	4	0.30	40.0M	10.0k
#7	1/4	1	2	0.27	39.7M	9.7k

Table 8: Various configurations of the MLP (Lower ENoPR ($\hat{\mathcal{L}}^1$) means higher capacity for representation). We report the computational cost (FLOPs) of the PWTP module

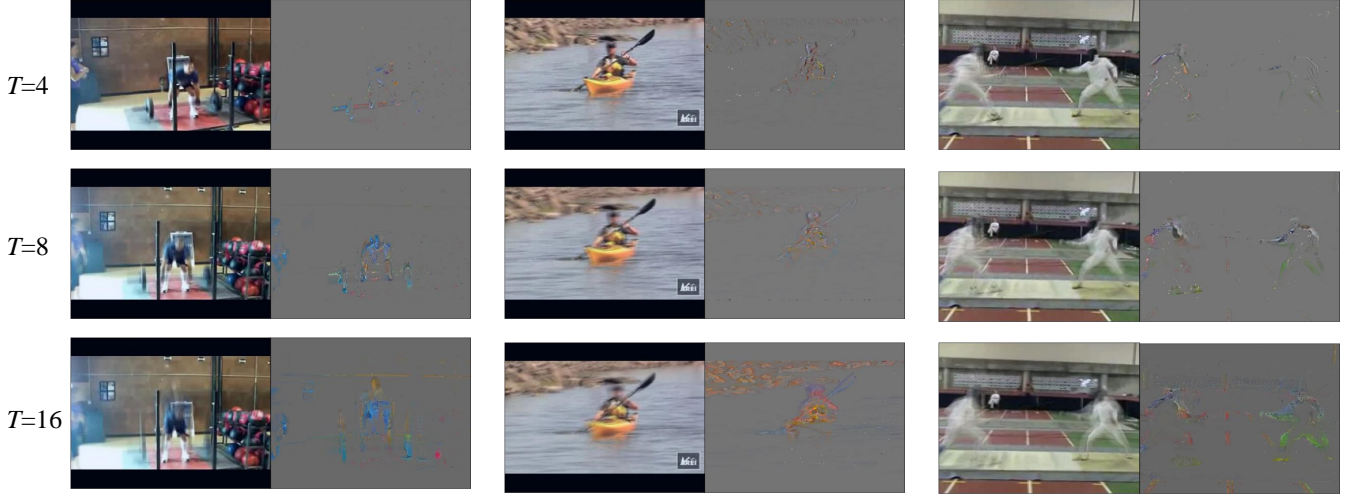


Figure 9: Example videos of different lengths (T) visualized as their frame averaging and corresponding dynamic appearances.

Scale Scheduler	ENoPR ($\hat{\mathcal{L}}^1$)	Accuracy (%)
$\gamma = 0.1, \lambda = 0.1$	0.57	40.7
$\gamma = 0.2, \lambda = 0.1$	0.53	40.6
$\gamma = 0.2, \lambda = 0.3$	0.56	40.7
$\gamma = 0.5, \lambda = 0.3$	0.55	40.4

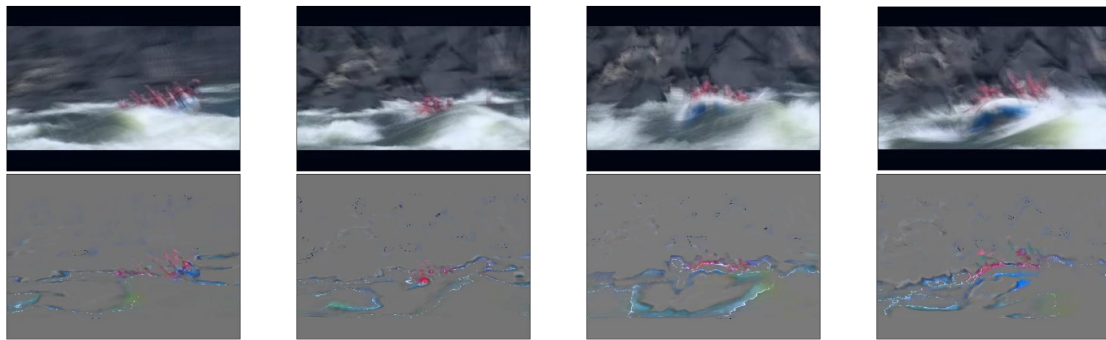
Table 9: Joint training with the Scale Scheduler on Something Something V1

T	ENoPR ($\hat{\mathcal{L}}^1$)	Accuracy
4	0.26	56.2
8	0.41	56.9
16	0.53	58.2

Table 10: Evaluating dynamic appearances generated with various temporal lengths T on Mini-Kinetics.

vide the averaging of sets of frames from video-clips and underneath their corresponding Dynamic Appearances. From these results, containing a wide range of videos, with 2 examples from each of UCF, Something Something V1, Kinetics

and HMDB database, we can observe that the dynamic appearance extracted by PWTP retains the essence of movement for a wide range of actions.



Rafting (UCF)



Juggling Balls (UCF)



Pretending to close something without actually closing it (SS)



Moving something up (SS)

Figure 10: Example videos of 4 segments visualized as their frame averaging and corresponding dynamic appearances.



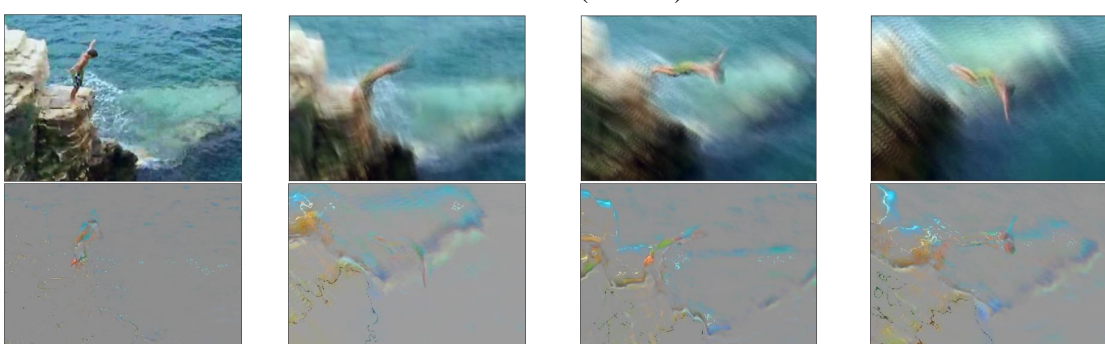
Tango dancing (Kinetics)



Riding a bike (Kinetics)



Brush hair (HMDB)



Dive (HMDB)

Figure 11: Example videos of 4 segments visualized as their frame averaging and corresponding dynamic appearances.